

Adsorption of molecular iodine on the Ag(111) surface: Phase transitions, silver reconstruction, and iodide growth

Cite as: J. Chem. Phys. **156**, 164702 (2022); <https://doi.org/10.1063/5.0089915>

Submitted: 01 March 2022 • Accepted: 05 April 2022 • Accepted Manuscript Online: 06 April 2022 •
Published Online: 25 April 2022

 B. V. Andryushechkin and  T. V. Pavlova



View Online



Export Citation



CrossMark

ARTICLES YOU MAY BE INTERESTED IN

[WSXM: A software for scanning probe microscopy and a tool for nanotechnology](#)

Review of Scientific Instruments **78**, 013705 (2007); <https://doi.org/10.1063/1.2432410>

[On-surface formation of metal-organic coordination networks with C \$\cdots\$ Ag \$\cdots\$ C and C=O \$\cdots\$ Ag interactions assisted by precursor self-assembly](#)

The Journal of Chemical Physics **154**, 044703 (2021); <https://doi.org/10.1063/5.0038559>

[Dehydrogenation of methanol on Cu₂O\(100\) and \(111\)](#)

The Journal of Chemical Physics **146**, 244702 (2017); <https://doi.org/10.1063/1.4989472>

Lock-in Amplifiers
up to 600 MHz



Zurich
Instruments



Adsorption of molecular iodine on the Ag(111) surface: Phase transitions, silver reconstruction, and iodide growth

Cite as: J. Chem. Phys. 156, 164702 (2022); doi: 10.1063/5.0089915

Submitted: 1 March 2022 • Accepted: 5 April 2022 •

Published Online: 25 April 2022



View Online



Export Citation



CrossMark

B. V. Andryushechkin^{1,2,a)}  and T. V. Pavlova¹ 

AFFILIATIONS

¹ Prokhorov General Physics Institute of the Russian Academy of Sciences, Vavilov Str. 38, 119991 Moscow, Russia

² HSE University, Myasnitskaya Str. 20, 101000 Moscow, Russia

^{a)} Author to whom correspondence should be addressed: andrush@kapella.gpi.ru

ABSTRACT

Room temperature adsorption of molecular iodine on Ag(111) has been studied by scanning tunneling microscopy (STM), low energy electron diffraction, Auger electron spectroscopy with factor analysis, and density functional theory (DFT). At the chemisorption stage, iodine first forms a $(\sqrt{3} \times \sqrt{3})R30^\circ$ structure. Further iodine dosing leads to continuous commensurate–incommensurate phase transition, taking place via the formation of striped superheavy domain walls. As a result, the uniaxially compressed $(13 \times \sqrt{3}-R30^\circ)$ phase is formed at an iodine coverage (θ) of 0.38 ML. At $\theta > 0.38$ ML, first-order phase transition begins, leading to the formation of hexagonal moiré-like phases, which exhibit an anomalously large corrugation in STM (0.8–2.3 Å). In the range of 0.40–0.43 ML, the compression of hexagonal phases occurs, which ends at the formation of the $(7 \times 7)R21.8^\circ$ structure at saturation. The DFT calculations allow us to explain the anomalous atomic corrugation of the hexagonal phases by the strong violation of the atomic structure of the substrate including up to ten layers of silver. Iodine dosing above 0.43 ML leads to the growth of 2D islands of silver iodide. The STM images of the silver iodide surface demonstrate a clear visible hexagonal superstructure with a periodicity of 25 Å superimposed with a quasi-hexagonal atomic modulation. DFT calculations of the atomic structure of AgI islands point to the formation of a sandwich-like double layer honeycomb structure similar to the case of I/Ag(100).

Published under an exclusive license by AIP Publishing. <https://doi.org/10.1063/5.0089915>

I. INTRODUCTION

Interaction of halogens with metal surfaces has been a subject of numerous investigations since the 1970s.^{1–3} The interest in halogen–metal interactions was stimulated by their important role in catalysis and microelectronics. It has been shown that halogens form a great variety of chemisorbed phases on metal surfaces. As a rule, the initial halogen adsorption leads to the formation of a simple commensurate structure, which transforms into the complex incommensurate structures at further adsorption. In this connection, halogens on metals can be considered as a good model system for studying 2D structural phase transitions in adsorbed monolayers.³

Attempts to study the atomic structure of iodine on the Ag(111) surface have been made several times. The first structural studies under the ultra-high vacuum (UHV) conditions were carried out in 1970–1980s by surface extended x-ray absorption fine structure

(SEXAFS),^{4–6} low energy electron diffraction (LEED),⁷ and photoelectron diffraction (PhD).⁸ In these works, the authors found that a commensurate structure $(\sqrt{3} \times \sqrt{3})R30^\circ$ is formed at the first stage of iodine adsorption. It has been reliably established that iodine occupies hollow sites; however, the unambiguous assignment of adsorption centers to either fcc or hcp positions failed.⁴ According to Bardi and Rovida,⁷ further adsorption of iodine leads to uniaxial compression of the iodine lattice at the first stage, and the formation of a uniformly compressed hexagonal lattice rotated by $\approx 3^\circ$ with respect to the $\langle 112 \rangle$ direction of the substrate at the second stage. This phase sequence was confirmed by surface x-ray diffraction (SXS) for iodine monolayers formed in the electrochemical cell.⁹ The real-space scanning tunneling microscopy (STM) measurements for the I/Ag(111) system were carried out only in the electrochemical cell.¹⁰ The authors were able to observe in STM a uniaxially compressed iodine lattice and a hexagonal moiré-like phase corresponding to a close-packed compressed iodine layer

rotated by $3.7^\circ \pm 1.0^\circ$ with respect to the $\langle 112 \rangle$ direction of the Ag(111) lattice.¹⁰

The structure and phase diagram of iodine adsorbed on Ag(111) is to some extent comparable to that of physisorbed rare gas adlayers on graphite¹¹ and single-crystal metal surfaces.^{12,13} Indeed, I/Ag(111) can be viewed as a model system to study 2D phenomena, such as commensurate–incommensurate (C-I) phase transitions of the surface structures. It is also noteworthy that the form and corrugation of the observed moiré-like superlattice in Ref. 10 are reminiscent of the “charge-density waves” observed by STM and diffraction methods at semiconductors and (to a smaller extent) on metal surfaces.¹⁴ Additional interest to the I/Ag(111) system concerns the process of the thin silver iodide film growth. Indeed, the growth of AgI after prolonged I₂ dosing on the Ag(111) surface was reported by Bardi and Rovida.⁷ The structure of the AgI film on the Ag(111) surface is of the great interest, taking into account the unusual sandwich-like structure of silver iodide found in the case of iodine adsorption on Ag(100)¹⁵ and recently attributed to a new class of 2D structures called the double layer honeycomb (DLHC) structure.¹⁶

In the present work, we examined the I/Ag(111) system with ultra-high vacuum scanning tunneling microscopy, low energy electron diffraction, Auger electron spectroscopy (AES), and density functional theory (DFT) calculations. We found out that the compression of the commensurate ($\sqrt{3} \times \sqrt{3}$)R30° layer occurs via the formation of the striped superheavy domain walls. In addition, we demonstrated that the rotated hexagonal phases exhibit moiré-like patterns with abnormally large corrugation equal to 0.8–2.3 Å, which is incompatible with a simple overlayer model. The problem was solved using extensive DFT calculations that reveal an extreme plasticity of silver under the iodine layer, which resulted in a complex surface reconstruction involving ≈ 10 layers of silver. STM measurements performed for the 2D AgI film grown on Ag(111) reveal the presence of another moiré-like superstructure with a period about 25 Å on the iodide surface in addition to the atomic modulation. The analysis of the AgI structure was performed with the help of DFT calculations. As a result, the DLHC sandwich-like model was confirmed for the I/Ag(111) system. It was also established that “sandwich” is separated from Ag(111) by a hexagonal buffer layer, which planar periodicity corresponds to the periodicity of the overlying iodide layer.

II. EXPERIMENTAL AND COMPUTATIONAL DETAILS

Experiments were carried out in an UHV setup consisting of analytical and structural analysis chambers. The analytical chamber is equipped with a cylindrical mirror electron analyzer (RIBER OPC-200) for Auger electron spectroscopy. The structural analysis chamber contains three-grid optics (VG RVL 640) for LEED measurements and a scanning tunneling microscope (GPI-300, Sigma Scan Ltd.). The base pressure in both chambers did not exceed 1×10^{-10} Torr.

The silver sample (Surface Preparation Laboratory) was cut parallel to the (111) plane with an accuracy better than 0.1° . To clean the surface, we used repetitive cycles of argon ion bombardment (1 keV) and annealing at 800 K. Tungsten tips sharpened *in situ* by Ar⁺ bombardment were used for STM measurements.

Iodine adsorption and STM measurements were carried out at room temperature. I₂ adsorption was carried out using a fine leak piezo-valve via a capillary placed near the sample surface. Before each new STM measurement, the sample was cleaned and dosed again with iodine. The iodine coverage was monitored by the intensity ratio (η) of I M_{4,5}VV (495–540 eV) and Ag M_{4,5}VV (335–365 eV) Auger peaks. To follow the changes of chemical states on a surface during iodine adsorption, factor analysis treatment of Auger spectra (AES-FA) was applied.^{15,17,18} For the treatment of the STM images, freeware software WSxM¹⁹ was used.

DFT calculations were carried out using the Vienna *ab initio* simulation package (VASP)^{20–23} employing the projector augmented wave method²⁴ and GGA-PBE (Perdew, Burke, Ernzerhof generalized gradient approximation) functional.²⁵

The integration over Brillouin zone was done using Monkhorst–Pack²⁶ k-point mesh $6 \times 4 \times 1$ [for the (2×3) cell], $1 \times 12 \times 1$ [for the $(25 \times \sqrt{3}$ -R30°) cell], $2 \times 12 \times 1$ [for the $(13 \times \sqrt{3}$ -R30°) cell], and $3 \times 3 \times 1$ [for the (7×7) R21.8° and $(\sqrt{79} \times \sqrt{79})$ R17.0° cells].

In most cases, the Ag(111) surface was represented by a 13-layer slab. As expected, to reduce the total number of atoms in the calculation, we used a six-layer slab for the $(25 \times \sqrt{3}$ -R30°) cell and seven-layer slab for the $(\sqrt{79} \times \sqrt{79})$ R17.0° cell. In all cases, the bottom two layers were fixed at bulk positions while positions of atoms in the remaining silver and iodine layers were allowed to relax. A vacuum gap between the slabs with a thickness of 15 Å was used in all calculations. STM simulations were performed within the Tersoff–Hamann approximation²⁷ using the Hive program.²⁸

III. RESULTS

A. AES and LEED data

Figure 1 presents results obtained by Auger electron spectroscopy in the course of the adsorption of molecular iodine on the Ag(111) surface at 300 K. Figure 1(a) shows the dependence of the ratio of the intensities of the Auger lines of iodine M_{4,5}VV and silver M_{4,5}VV (η) on the dosing time (t). During I₂ dosing, the pressure increase in the chamber was 2×10^{-10} Torr, which approximately corresponds to the local iodine pressure near the sample surface of $1\text{--}2 \cdot 10^{-8}$ Torr. It can be seen that the rapid growth of η in the initial region of adsorption is then replaced by a slower growth of the signal. The saturation level of the adsorption curve is $\eta = 0.54$ [Fig. 1(a)]. The saturation of the curve in Fig. 1(a) corresponds to the formation of an unbroken AgI film with a thickness d exceeding the mean free path of Auger electrons ($d > 25$ Å). Although the Auger-peak intensity ratio does not carry information about various chemical states on the surface, it can be used as a measure of the total number of iodine atoms on the Ag(111) surface.

Step-by-step adsorption of iodine on the silver surface leads to a change in the chemical state of the surface, which is reflected in the change in the shape and positions of the Auger lines of silver and iodine. To correctly extract information on the chemical state of atoms on the surface from the Auger spectra, we used factor analysis,¹⁷ which made it possible to decompose the Auger spectra into components and obtain concentration dependencies for

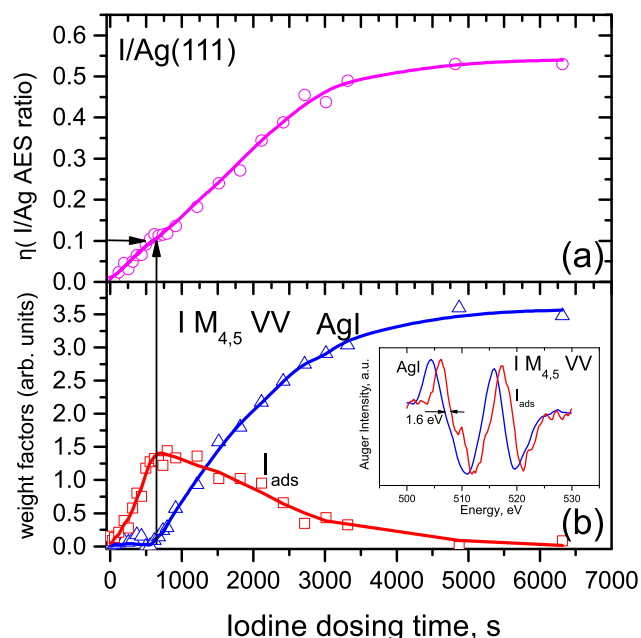


FIG. 1. AES data obtained for adsorption of molecular iodine on the Ag(111) surface at 300 K. (a) Dependence of the $I(M_{4,5}VV)/Ag(M_{4,5}VV)$ AES ratio (η) on the I_2 adsorption time [the local pressure of iodine near the sample face was in the range of $(1-2) \cdot 10^{-8}$ Torr]. (b). Graphical representation of the results of factor analysis of Auger spectra for the iodine line. The weights of AgI and I_{ads} components are indicated in red and blue, respectively. The inset of (b) presents standard $I M_{4,5}VV$ spectra for chemisorbed iodine (blue line) and silver iodide (red line).

each component separately. For the I/Ag(111) system, factor analysis identified two main components: chemisorbed iodine and silver iodide.

Figure 1(b) shows the intensities of the iodine Auger line components depending on the time of molecular iodine dosing. The inset of Fig. 1(b) shows the normalized standard $I M_{4,5}VV$ Auger spectra corresponding to chemisorbed iodine (I_{ads}) and iodine in the AgI film, which were used as a reference in the factor analysis procedure. The spectrum at time $t = 500$ s was taken as the reference spectrum of chemisorbed iodine, so up to $t < 630$ s, the factor analysis indicates that I_{ads} is the only component in the system. To obtain the reference spectrum of AgI, an additional 5 min exposure of I_2 was made at a local pressure near the sample surface of 1×10^{-7} Torr, which guaranteed the formation of an iodide film with a thickness significantly exceeding the Auger electron escape depth. At the first stage of adsorption, the chemisorbed state (I_{ads}) is filled. It also follows from Fig. 1(b) that the growth of silver iodide begins at $t \approx 630$ s and corresponds to saturation of the chemisorbed iodine coverage with $\eta = 0.1$. Then, with further adsorption of iodine, the intensity of the AgI component increases, saturating at $\eta = 0.54$. In turn, the intensity of the component corresponding to chemisorbed iodine (I_{ads}) gradually decreases starting from $t > 630$ s and becomes equal to zero, simultaneously with the saturation of the AgI signal.

Figure 2 presents a series of diffraction patterns obtained in the course of the continuous exposure of molecular iodine onto the

Ag(111) surface at 300 K. The LEED pattern that develops first is $(\sqrt{3} \times \sqrt{3})R30^\circ$ [Fig. 2(a)]. The increase of the iodine coverage resulted in broadening [Fig. 2(b)] and subsequent splitting of the $\sqrt{3}$ -spots into six-spot triangles [Fig. 2(c)] in good correspondence with data by Bardi and Rovida.⁷ Figure 2(d) shows the diffraction pattern with the maximum size of triangles. Further iodine dosing leads to the formation of a complex “horseshoe”-type structure [Fig. 2(e)], after which rosettes of six spots are formed around former $(\sqrt{3} \times \sqrt{3})R30^\circ$ spot positions, the size of which grows with the coverage [Figs. 2(f)–2(i)]. All these transformations generally agree with the data by Bardi and Rovida.⁷

It is noteworthy that all the transformations visible in the diffraction pattern take place within a very narrow interval of iodine coverage characterized by $\eta \approx 0.08-0.10$.

B. STM data

1. The $(\sqrt{3} \times \sqrt{3})R30^\circ$ phase

Figure 3(a) shows an atomic-resolution STM image of the clean Ag(111) surface. The STM image of the iodinated surface corresponding to a sharp $(\sqrt{3} \times \sqrt{3})R30^\circ$ LEED pattern [Fig. 2(a)] is presented in Fig. 3(b). A clearly seen the hexagonal lattice with a period of 5 Å is naturally assigned to a simple commensurate $(\sqrt{3} \times \sqrt{3})R30^\circ$ structure with one iodine atom per unit mesh (with an exact coverage of 0.33 ML).

Our DFT calculations performed for the $(\sqrt{3} \times \sqrt{3})R30^\circ$ structure showed that the most energetically preferable adsorption site of the iodine atom on Ag(111) corresponds to the fcc hollow position ($E_a = -1.81$ eV). The adsorption energies for hcp and top sites were found to be -1.80 and -1.59 eV, respectively. The bridge position of the iodine atom appears to be unstable.

Since the interatomic distances in the $(\sqrt{3} \times \sqrt{3})R30^\circ$ lattice appear to be much larger than the van der Waals diameter of iodine ($4.0-4.1$ Å²⁹⁻³¹), the increase of the coverage above 0.33 ML results in the compression of the iodine layer, as it follows from previous studies.^{7,10} However, the mechanism of iodine lattice compression has not been well-described so far. In this connection, the phase transitions in the iodine monolayer on Ag(111) need to be studied in detail with STM and DFT.

2. Uniaxially compressed phases

Figures 4(a)–4(d) show STM images of iodine phases corresponding to the coverage exceeding 0.33 ML and exhibiting “triangle” LEED patterns as shown in Figs. 2(b)–2(d). In addition to the atomic structure, STM images clearly show modulation consisting of alternating dark and light stripes, the direction of which coincides with one of the directions of closely packed rows of iodine atoms in the $(\sqrt{3} \times \sqrt{3})R30^\circ$ phase ($\langle 112 \rangle$). For STM images shown in Figs. 4(a)–4(d), the modulation period is decreasing with the iodine coverage from 50 Å down to 19 Å. Linear modulation means that the symmetry of the adsorbate (iodine) structure and the lattice symmetry of the Ag(111) substrate are different. The average interatomic distance along the direction of the stripes is equal to ≈ 5.0 Å coinciding with the I–I distance in the $(\sqrt{3} \times \sqrt{3})R30^\circ$ phase, while average distances along the other two close-packed atomic rows appear to be lower. Therefore, the uniaxial compression of the iodine lattice becomes evident.

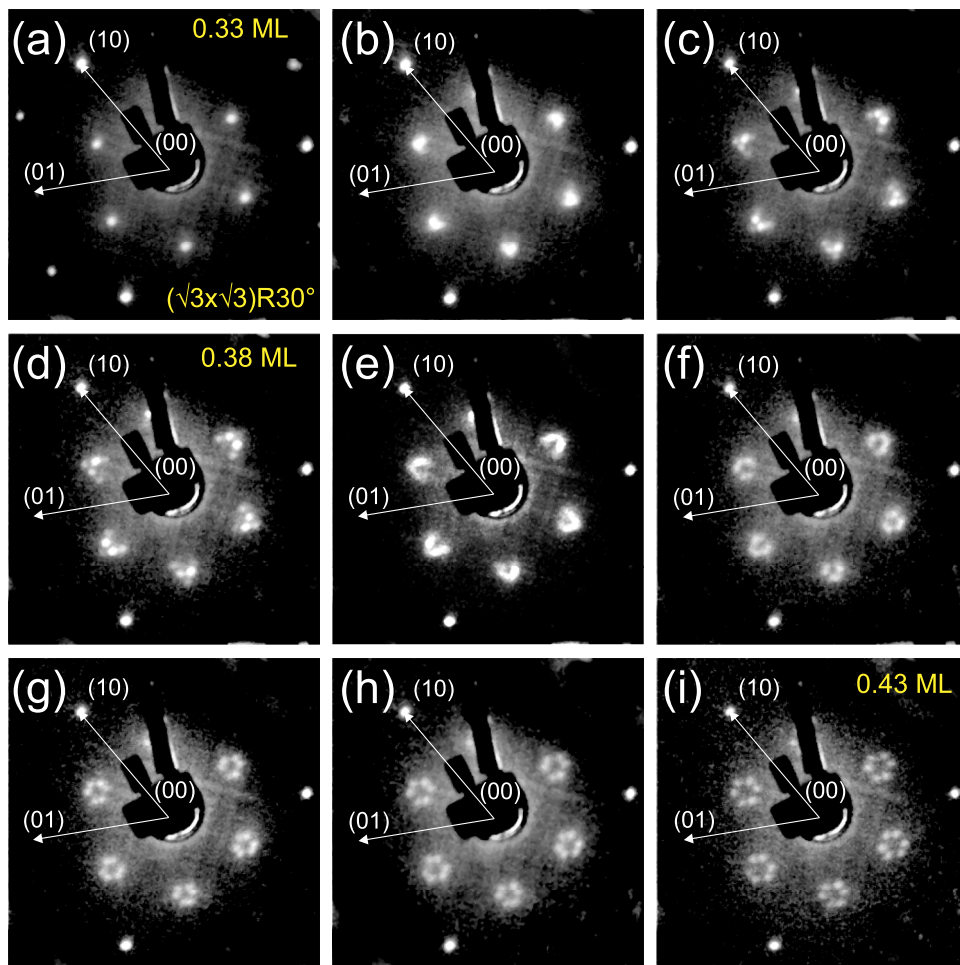


FIG. 2. Evolution of the LEED pattern ($E_0 = 84$ eV) during continuous iodine adsorption on the Ag(111) surface at 300 K. The reciprocal lattice vectors of the silver surface are shown. (a) Sharp Ag(111)- $(\sqrt{3} \times \sqrt{3})R30^\circ$ -I pattern; (b)–(d) development of the “triangle” pattern, (e) “horseshoe”-type structure, (f)–(h) development of “rosette” pattern, and (i) final “rosette” pattern corresponding to the saturated layer of iodine.

The interatomic distances in the dark stripes (5 \AA) are the same as in the $(\sqrt{3} \times \sqrt{3})R30^\circ$ structure, while in the bright stripes, they are lower ($4.5\text{--}4.9 \text{ \AA}$). We believe that the striped structure in Fig. 4 reflects the formation of regular spaced striped domain walls

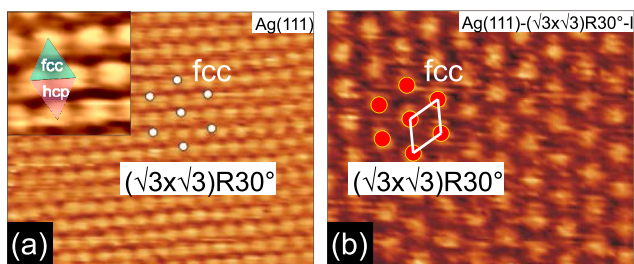


FIG. 3. (a) Atomic-resolution STM image ($44 \times 37 \text{ \AA}^2$, $I_t = 0.4$ nA, $U_s = -9$ mV) of the clean Ag(111) surface. (b) STM image ($44 \times 37 \text{ \AA}^2$, $I_t = 0.2$ nA, $U_s = 500$ mV) of the $(\sqrt{3} \times \sqrt{3})R30^\circ$ phase formed on Ag(111) at the coverage of 0.33 ML. The inset of (a) demonstrates fcc and hcp adsorption sites on the Ag(111) surface. Positions of iodine atoms are shown by red balls. The $(\sqrt{3} \times \sqrt{3})R30^\circ$ unit cell is indicated in both (a) and (b).

separating the $(\sqrt{3} \times \sqrt{3})R30^\circ$ domains. We assign the light areas to the domain walls. The Fourier transforms of the STM image shown in right parts of Figs. 4(a)–4(d) demonstrate the uniaxial splitting of the spots around former, $(\sqrt{3} \times \sqrt{3})R30^\circ$ spot positions, with the magnitude of splitting increasing with the iodine coverage. Due to the symmetry of the substrate, the compression of the iodine lattice can occur in three equivalent directions, rotated with respect to each other by 120° , as shown in Fig. 4(e).

Taking into account the low spatial resolution of the electron beam, we can conclude that the LEED patterns will always contain a contribution from domains with different compression directions. Figure 4(e) shows a schematic indicating that a typical six-spots LEED pattern can be explained by the simultaneous contribution of three domains.

To describe the structure in detail, we performed DFT modeling of two striped phases corresponding to the modulation period of 36 and 19 \AA [see Figs. 4(b) and 4(d)]. Figures 5(a)–5(c) presents analysis of the low coverage ($25 \times \sqrt{3}$ - $R30^\circ$) phase. Figure 5(a) shows an experimental STM frame. A theoretical STM image and DFT optimized model are shown in Figs. 5(b) and 5(c), respectively. One can see that iodine atoms in dark stripes occupy fcc hollow positions, while atoms in the bright stripes appear to be in positions

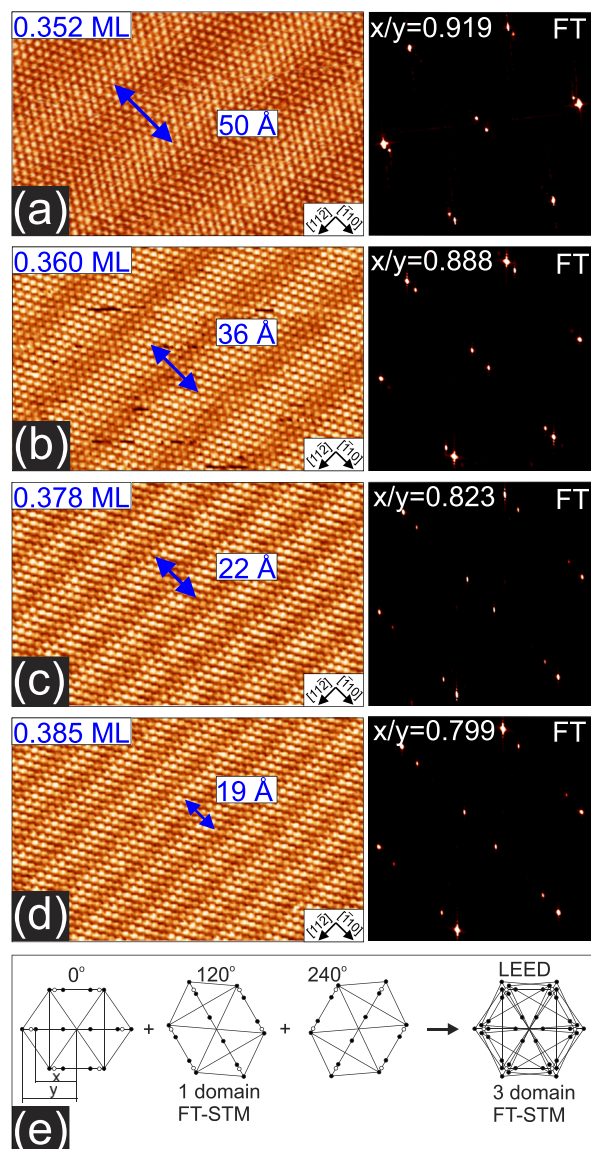


FIG. 4. (a)–(d) Atomic-resolution STM images ($190 \times 121 \text{ \AA}^2$, $I_t = 0.3 \text{ nA}$, $U_s = -940 \text{ mV}$, 300 K) and corresponding Fourier transforms (FT) of the striped phases observed during continuous adsorption of iodine on $\text{Ag}(111)$ for the coverage exceeding $1/3$ of a monolayer. Splitting in FT and LEED is characterized by the ratio x/y as shown in (e). The iodine coverage is indicated in each STM-frame. (e) The model drawing explaining the appearance of triangles of six-spots in LEED and FT-STM. Due to the substrate symmetry, there are three possible orientations of the uniaxially compressed domains, as shown on the left. Positions of spots are shown by black circles. The open circles correspond to spots in the $(\sqrt{3} \times \sqrt{3})R30^\circ$ structure. Due to the relatively large size of the electron beam in LEED, the resulting diffraction pattern, shown on the right, will always contain contributions of all three domains with different orientations.

close to bridge or hcp. Therefore, our data point to the formation of the network of the antiphase $(\sqrt{3} \times \sqrt{3})R30^\circ$ domains (dark stripes) separated by domain walls (bright stripes). The phase shift between neighboring domains corresponds to super-heavy striped

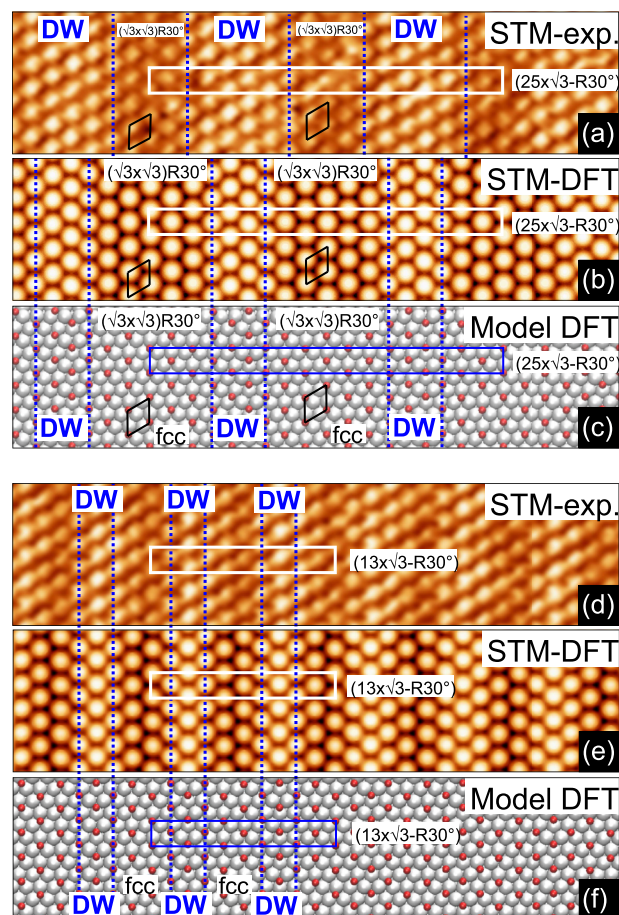


FIG. 5. (a) and (d) STM images ($124 \times 29 \text{ \AA}^2$; $I_t = 0.2 \text{ nA}$, $U_s = -500 \text{ mV}$) corresponding to the striped structures with periods of $\approx 36 \text{ \AA}$ (a) and $\approx 19 \text{ \AA}$ (d). The $(25 \times \sqrt{3}\text{-}R30^\circ)$ and $(13 \times \sqrt{3}\text{-}R30^\circ)$ unit cell are indicated; (b) and (e) Theoretical STM images of the $(25 \times \sqrt{3}\text{-}R30^\circ)$ and $(13 \times \sqrt{3}\text{-}R30^\circ)$ structures ($U_s = -500 \text{ mV}$); (c) and (f) The DFT-optimized models of the $(25 \times \sqrt{3}\text{-}R30^\circ)$ and $(13 \times \sqrt{3}\text{-}R30^\circ)$ structures. Silver and iodine atoms are shown by white and red balls, respectively.

domain walls.³² The comparison of the experimental STM image with a calculated one reveals noticeable relaxation of the domain walls. Indeed, the domain wall in the theoretical STM image consists of four atomic rows, while in the experimental image, it is formed by at least six atomic rows. The analysis of the maximally compressed $(13 \times \sqrt{3}\text{-}R30^\circ)$ striped phase is presented in Figs. 5(d)–5(f). In this case, the $(\sqrt{3} \times \sqrt{3})R30^\circ$ domains are degenerated into two atomic rows (dark stripes), while the domain-wall width decreases to three atomic rows. It is noteworthy that the theoretical STM image and DFT optimized atomic structure model are in good agreement with a room temperature experiment indicating to the lack of the relaxation of atomic positions for highly compressed phase.

The broadening of the domain walls observed for less denser phase may be explained by the thermal fluctuations of atomic positions at finite temperature (300 K). In general, the observed

relaxation of domain walls, as well as their fluctuations, makes it difficult to accurately determine the modulation period and coverage directly from the STM data. However, this problem can be easily solved by analyzing the Fourier transform of an STM image. Indeed, the distance between domain walls is determined by the following expression: $l = a \cdot (2 + 1.5 \cdot n)^{33,34}$ [$n = 1, 2, 3 \dots$, and a is the lattice parameter of the substrate— 2.89 \AA for Ag(111)]. Splitting of spots on the Fourier transform can be described by the ratio x/y [see the model in Fig. 4(e)], which is equal to $(n + 1)/(n + 2)$. For the most compressed structure in Figs. 4(d) and 5(d), the experimental value of the splitting parameter x/y is equal to $0.80 \pm 0.01 \text{ \AA}$. It is clear that this value fits with the x/y ratio calculated for $n = 0$ and corresponds to the distance between domain walls $l = 2.89 \text{ \AA} \times (2 + 1.5 \times 3) = 18.79 \text{ \AA}$. The calculated value of l coincides with the distances between the stripes in Figs. 4(b) and 5(b). For super-heavy striped domain walls, the distance l and the coverage θ are coupled as $l = a/(3 \cdot \theta - 1)$.³⁴ Thus, it becomes possible to accurately calculate the coverage for the most compressed iodine phase as $\theta = 0.38 \text{ ML}$.

Another remarkable feature of the uniaxially compressed phases is a weak atomic corrugation not exceeding 0.2 \AA . This value correlates with the difference in the z -position for the iodine atom adsorbed in hollow and bridge sites.³⁵

3. Hexagonal moiré-like phases

To investigate the detailed scenario of iodine phase transformations on the Ag(111) surface, we dosed the sample with molecular

iodine during scanning directly in STM (Fig. 6). One can see that the increase of the iodine coverage above 0.38 ML leads to the first-order phase transition and the formation of the new hexagonal superstructure with a period of 28 \AA [Fig. 6(a)] coexisting with a striped ($13 \times \sqrt{3}\text{-R}30^\circ$) phase. The coexisting of two phases explains the diffraction pattern in Fig. 2(c) in which the horseshoe-like features are visible instead of the sharp reflexes.

At further dosing, the new superstructure fully replaces the ($13 \times \sqrt{3}\text{-R}30^\circ$) phase. Then, as iodine was adsorbed, the period of the superstructure decreases to the value $\approx 20 \text{ \AA}$, as seen in Figs. 6(c)–6(e).

The insets of Figs. 6(c)–6(e) show atomic resolution STM images of hexagonal moiré-like phases (hex.-20, hex.-25, hex.-28) with periods 28, 25 and 20 \AA , respectively. One can see that in all cases, the moiré-lattice appears to be rotated by a certain angle with respect to atomic rows. Such observation means the rotation of the iodine lattice with respect to the $\langle 112 \rangle$ direction of the Ag(111) substrate, which is consistent with the model proposed by Bardi and Rovida.⁷

Further information on the atomic structure of the hexagonal phases can be obtained by analyzing the Fourier transforms of STM images in comparison with the diffraction pattern. Fourier transforms in the insets of Figs. 6(c) and 6(e) are structurally similar but differ in the degree of splitting. The spots in the Fourier transform images can be divided into two groups. Six spots corresponding to the superstructure are clearly visible near the center. It can be seen that when the iodine lattice is compressed (Fig. 6), the period of the

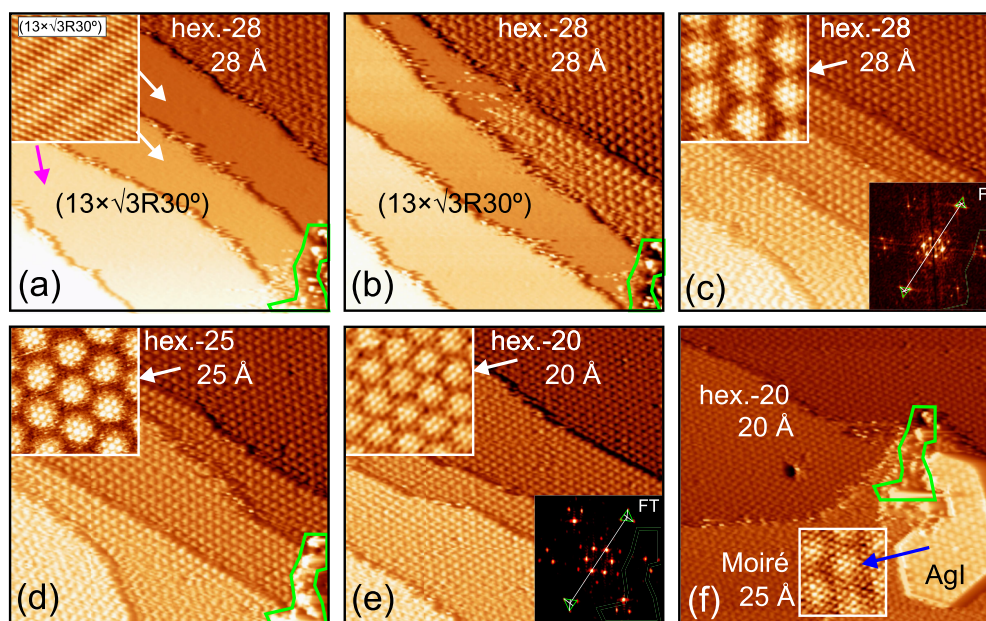


FIG. 6. Panoramic STM images ($780 \times 725 \text{ \AA}^2$, $I_t = 0.13 \text{ nA}$, $U_s = -1333 \text{ mV}$) acquired in the course of the continuous I_2 dosing of the Ag(111) surface demonstrating the appearance of the hexagonal superstructure and the nucleation of the AgI island. (a) and (b) The appearance of the high-corrugated hexagonal superstructure with a period of 28 \AA on the upper terraces. Smooth terraces still contain the striped ($13 \times \sqrt{3}\text{-R}30^\circ$) phase. (c) The occupation of the all surface area by the hexagonal phase with a period of 28 \AA . (d) and (e) Evolution of the hexagonal phase with iodine adsorption: the gradual decrease in the periodicity down to $\approx 20 \text{ \AA}$. (f) Nucleation of the AgI island near the surface defect. The STM image reveals a moiré-like pattern with a period of 25 \AA on the AgI surface, as seen in the inset. Atomic-resolution STM images of different hexagonal phases ($80 \times 80 \text{ \AA}^2$) are shown in (c)–(e). The contour of the same surface defect is shown in all STM frames in green.

superstructure decreases and the size of the corresponding hexagon in Fourier transform increases. The spots from the second group form triangles around $\sqrt{3}$ positions and correspond to the atomic corrugation of the surface. It should be noted that the axes of symmetry of the triangles are slightly rotated with respect to the lines passing through their centers.

In contrast to the Fourier images, the LEED pattern contains rosettes of six spots around the $\sqrt{3}$ -positions. The Fourier transform also can show six spots if we consider the STM image containing two different domains with the iodine lattice rotated clockwise or counterclockwise with respect to the $\langle 112 \rangle$ direction of Ag(111), as seen in Fig. 7. The centers of the rosettes correspond to the exact $\sqrt{3}$ spot positions, as follows from LEED.

Thus, the analysis of the STM-images containing two domains makes it possible to eliminate distortions in the STM image due to thermal drift and, therefore, to extract correct information from Fourier analysis. Using this approach, we determined that the family of the hexagonal moiré-like phases correspond to the hexagonal iodine lattices with average interatomic distances of 4.56–4.41 Å ($\theta = 0.40$ – 0.43 ML) and the angles of rotation with respect to the $\langle 112 \rangle$ direction in the range of $\pm(1.4$ – $2.7)^\circ$.

We should also emphasize that the amplitude of the surface corrugation for all hexagonal phases is equal to ≈ 0.8 – 2.3 Å depending on the tip sharpness, being in any case much larger than that for the striped phases. Of course, one should take into account the probable occupation of the on-top positions for the hexagonal phases. Nevertheless, such corrugation significantly exceeds the difference in height between fcc and top positions (≈ 0.3 – 0.4 Å) estimated on the base of DFT calculations³⁵ and “hardball contact model.”¹⁰

To solve this problem, we performed DFT calculations for the most compressed hexagonal phase with a period of about 20 Å. Since this phase is incommensurate with the substrate for calculations, we used a high-order commensurate structure (7×7)R21.8° with a period of 20.23 Å and the angle of rotation of 2.68°, as a closest approximation of the real structure. In the starting configuration, all iodine atoms were equally spaced within (7×7)R21.8° unit cell. The optimization of coordinates gave rise to unexpected behavior of the system. The iodine atom occupying position close to on-top presses the underlying silver atom into the bulk. This shift causes a significant perturbation in the positions of silver atoms of up to

a depth of 12 layers, as seen in Figs. 8(a) and 8(b). The neighboring silver atoms, on the contrary, shift up by ≈ 1 Å giving rise to a significant corrugation of the surface. Other iodine atoms appear to be adsorbed on such corrugated surfaces occupying positions close to threefold hollow sites [see Fig. 8(b)]. Figure 8(c) shows the theoretical STM image corresponding to the model in Fig. 8(b) and reproducing the experimental image of the most compressed moiré-like hexagonal phase presented in Fig. 8(d). The total corrugation measured in the theoretical STM image is about 2.2 Å. It is noteworthy that this value approximately corresponds to the maximum difference in z -positions for iodine atoms. However, in most of real experiments, the smoothing of corrugation occurs due to the finite size of the tip.

Thus, the anomalously strong corrugation observed in STM for all hexagonal phases is due to a large violation of the silver atomic structure caused by iodine adsorption. It is also noteworthy that this effect appears most clearly for calculations taking into account more than ten atomic layers of silver. The decrease in the z -size of the unit cell leads to the noticeable decrease in the surface corrugation down to 0.1–0.2 Å. In this connection, our result can be considered as an additional confirmation of the importance of the choice of an appropriate unit cell in DFT in order to reproduce real experimental observations.

4. AgI growth

After the formation of a superstructure with a period of 20 Å, new objects appear on the Ag(111) surface— islands located near atomic steps or in the vicinity of impurities or defects on the surface [Fig. 6(f)]. The island height measured in STM frames varies in the range from 4.0 to 4.5 Å depending on the tunneling voltage. Similar objects at $\eta < 0.10$ (the level of saturated iodine monolayer, see Fig. 1) were not observed, which makes it possible to identify these islands as silver iodide (AgI). A hexagonal atomic structure with a period of ≈ 4.6 Å is clearly visible on the surface of the island and a superstructure with an average period of ≈ 25 Å. As iodine adsorbs, the surface area occupied by AgI islands increases, while their height remains the same, i.e., one can speak about the 2D growth mode. The growth of AgI is accompanied by the significant mass transport

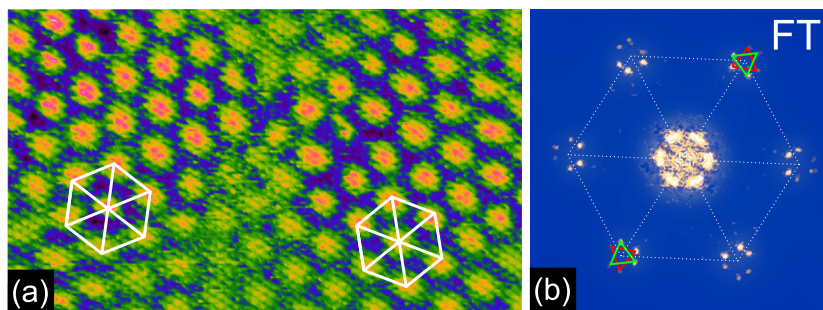


FIG. 7. (a) STM image (245×206 Å, $I_t = 0.15$ nA, $U_s = -700$ mV) of the most compressed hexagonal iodine phase (hex.-20) on Ag(111). Two domains with different orientations of the moiré lattice are clearly seen. (b) Fourier transform of the STM image from (a) exhibiting rosettes of six spots around the $(\sqrt{3} \times \sqrt{3})R30^\circ$ spot positions indicated by the dotted line contour. Green and red triangles shows the contributions from differently rotated domains.

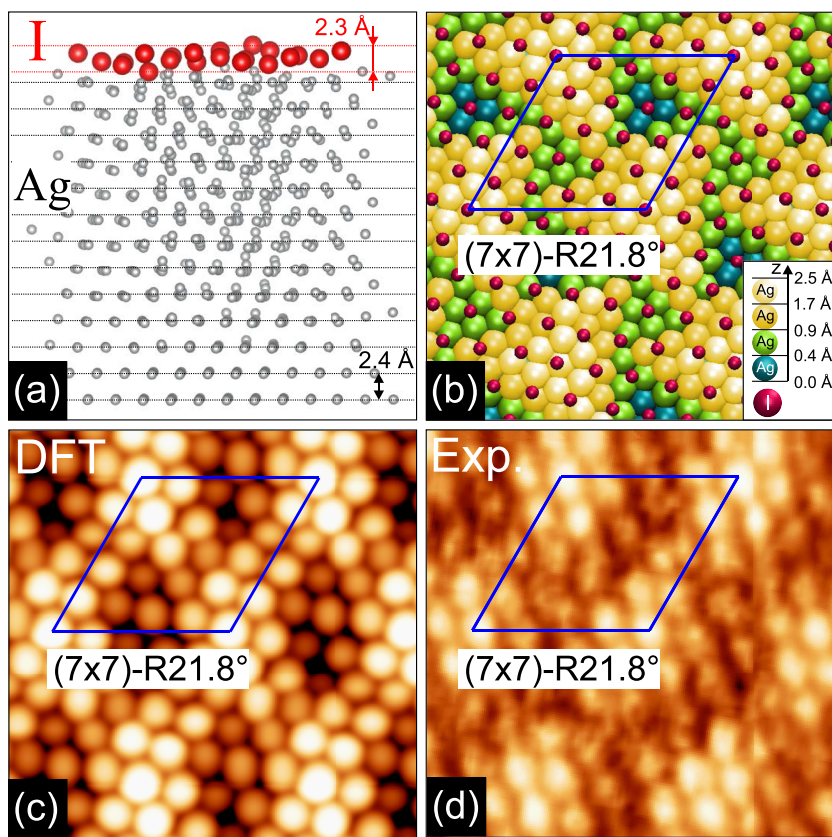


FIG. 8. (a) Side view of the atomic structure of the hexagonal $(7 \times 7)R21.8^\circ$ iodine phase on Ag(111). Silver atoms are shown by gray open circles. The positions of undisturbed silver planes are indicated by horizontal lines. The maximum amplitude of the iodine layer corrugation is also indicated. (b) Top view of the structure shown in (a). Silver atoms corresponding to different z coordinates are shown in different colors, according to the inset. Iodine atoms in (a) and (b) are shown in red. (c) Theoretical STM image ($47 \times 47 \text{ \AA}^2$, $U_s = -500 \text{ mV}$) of the $(7 \times 7)R21.8^\circ$ iodine phase corresponding to the optimized model presented in (a) and (b). (d) Experimental STM image ($47 \times 47 \text{ \AA}^2$, $I_t = 0.2 \text{ nA}$, $U_s = -500 \text{ mV}$) of the maximum compressed hexagonal phase. The $(7 \times 7)R21.8^\circ$ unit cell is indicated in (b)-(d) by blue color.

and steps shrinking, as seen in Fig. 6(d) and video presented in the supplementary material.

Figure 9(a) presents an STM image recorded with an atomic resolution showing both the surface of the iodide island and the terrace covered with the saturated iodine monolayer (hex.-20 phase). A hexagonal atomic structure with a period of $\approx 4.5\text{--}4.6 \text{ \AA}$ and a moiré superstructure with an average period of $\approx 25 \text{ \AA}$ are clearly visible on the island surface. The drift distortions were eliminated taking into account the known structure of the saturated hexagonal phase.

The analysis of Fourier transforms taken from each of two phases in the STM image shows almost complete coincidence of the directions of the closely packed atomic rows in hexagonal and AgI phases, as shown in Figs. 9(b)–9(d).

Now, we turn to analysis the origin of the moiré-like superstructure on the AgI surface. Usually, moiré-patterns arise due to the interference of the overlayer and underlying lattices. The moiré periodicity vectors \mathbf{m}_1 , \mathbf{m}_2 are related to vectors of the underlying lattice $(\mathbf{a}_1, \mathbf{a}_2)$ and the overlayer lattice $(\mathbf{b}_1, \mathbf{b}_2)$. The reciprocal vectors of

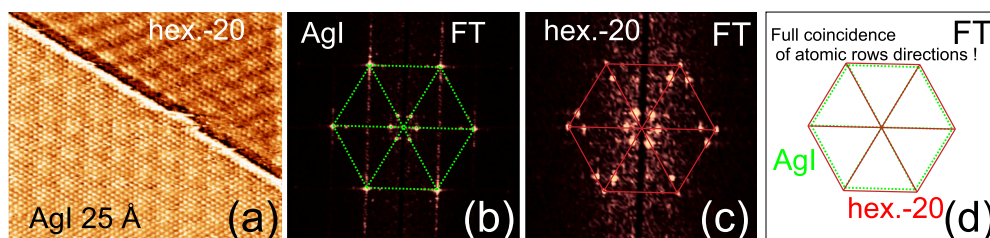


FIG. 9. (a) STM image ($227 \times 246 \text{ \AA}^2$, $I_t = 0.15 \text{ nA}$, $U_s = -400 \text{ mV}$), demonstrating the edge of the AgI island and the atomic terrace with the hex.-20 chemisorbed iodine phase. (b) and (c) FT images of STM frames containing only silver iodide and the hex.-20 phase, respectively. (d) The superimposition of the Fourier transformation images for AgI and the hex.-20 phase. The full coincidence of three base directions in both hexagons means the coincidence of the close-packed atomic rows in hex.-20 phase and silver iodide.

m_1 , m_2 must be given by a linear combination of the reciprocal vectors of a_1 , a_2 and b_1 , b_2 . The overlayer lattice corresponds to the slightly expanded silver iodide lattice since it is clearly visible in STM images. As for the underlying lattice, two scenarios are possible. In the first case, the underlying lattice could be an interface for the iodine layer preserving the structure of the saturated iodine monolayer, i.e., the hexagonal iodine layer on the corrugated silver (111) surface. In the second case, no interface layer exists between iodide and the substrate and the moiré pattern arises due to the interference of the iodide and substrate lattices.

It is noteworthy that first scenario seems to be plausible from the first view, since it is realized in a number of the halide/metal systems: CuI/Cu(100),³⁶ CuI/Cu(111),³⁶ CuI/Cu(110),³⁷ AgI/Ag(100),¹⁵ NiI₂/Ni(100),³⁸ and NiI₂/Ni(110).³⁹ However, this is not the case since the saturated iodine monolayer in the first approximation is described by the hexagonal lattice with a I–I distance of 4.41 Å and the interatomic distances in AgI are equal to ≈4.6 Å. Since the directions of the closely packed atomic rows in both phases coincide, as seen from Fig. 9(c), the resulting moiré-pattern period would be equal to ≈97 Å that is not in line with the experiment.

If the “interface” layer is absent (second scenario), the substrate plays the role of the underlayer. Taking into account the difference in length of the substrate ($a_{Ag_1}^*$, $a_{Ag_2}^*$) and iodide vectors (b_1^* , b_2^*), the appropriate moiré vectors (m_1^* , m_2^*) in this case can be calculated using the following formulas:

$$\begin{aligned} m_1^* &= 2b_1^* - b_2^* - a_{Ag_1}^*, \\ m_2^* &= b_1^* + b_2^* - a_{Ag_2}^*. \end{aligned} \quad (1)$$

In particular, if the AgI lattice is described by the high-order commensurate ($\sqrt{79} \times \sqrt{79}$)R17.0° unit cell, the period of the superstructure will be equal to 25.7 Å. In this model used in our DFT calculations, the interatomic distances in the plane of AgI are equal to 4.61 Å and the angle of the rotation with respect to the <112> direction of 4°.

Let us now turn to a theoretical analysis of the structure of AgI islands on the Ag(111) surface using *ab initio* DFT calculations. In the beginning, it is necessary to consider the structure of the bulk AgI crystal, which, under normal conditions, has two crystalline phases: the wurtzite type (β -phase, $a = 4.580$ Å, $c = 7.494$ Å⁴⁰) and the zinc blende type (γ -phase, $a = 6.473$ Å). The β -AgI and γ -AgI crystals in the <0001> and <111> directions, respectively, consist of a sequence of alternating hexagonal Ag–I bilayers. In this case, the irreducible cell for β -AgI consists of two bilayers and that for γ -AgI consists of three bilayers. It should be noted that the I–Ag interplanar distances in bilayers (0.94 Å) and the distances between bilayers in the β - and γ -phases (2.81 Å) coincide within 0.01 Å. The lattice parameters in the (0001) plane for the β -phase and in the (111) hexagonal planes for the γ -phase also coincide with a very high accuracy (4.577 and 4.580 Å).⁴⁰

In 2009, Andryushechkin *et al.*¹⁵ have demonstrated that the atomic structure of the thin AgI film growing on Ag(100) as a result of I₂ adsorption does not correspond to either β - or γ -phases. According to the DFT calculations, the silver iodide islands on Ag(100) consist of four hexagonal atomic planes parallel to the substrate surface. They are arranged in the “sandwich”-structure, containing two coupled silver planes in the middle and iodine planes

on each side. The sandwich as a whole is situated on top of the $c(2 \times 2)$ iodine monolayer, which remains as the atomically sharp interface between AgI and the substrate.

In this connection, it is reasonable to assume that the sandwich structure can be realized also in the case of AgI/Ag(111). For our DFT calculations, first, we took two double bilayer configurations corresponding to β - and γ -phases placed on the clean Ag(111) surface. The optimization of coordinates resulted in the breakdown of the initial configurations and the formation of the structures incompatible with the experiment. Such a result points to the necessity to modify our model and introduces a buffer iodine layer between the two-bilayer film and the substrate. Since the moiré periodicity on the AgI surface corresponds to the interference of the Ag(111) and AgI lattices, the in-plane parameters of the buffer iodine layer should correspond to ones in the hexagonal planes of AgI. Therefore, the buffer layer appears to be less dense than the saturated iodine monolayer in the hexagonal phase.

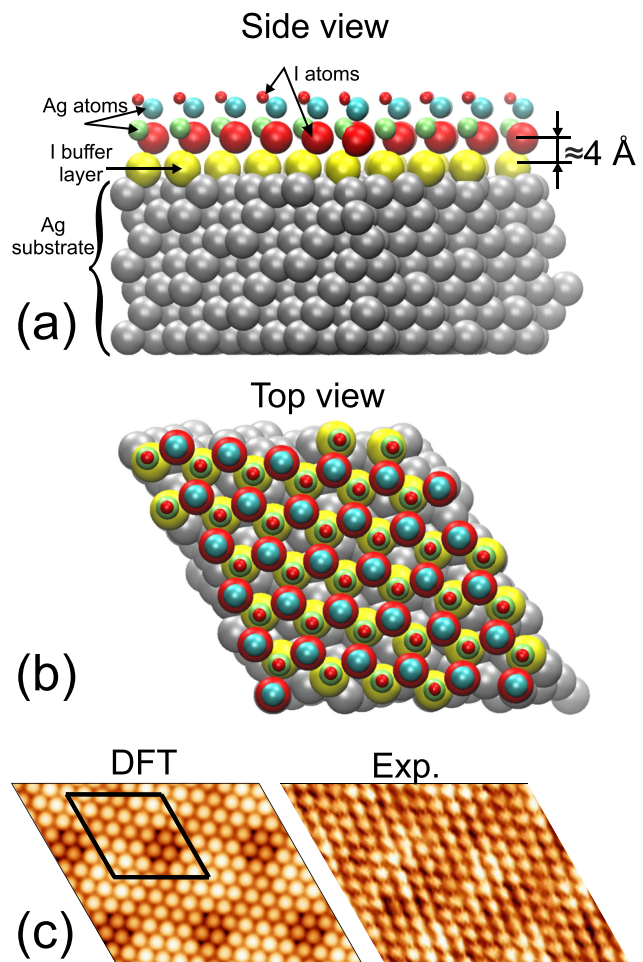


FIG. 10. Top (a) and side (b) views on the sandwich-like DLHC structure of the AgI film obtained as a result of the DFT calculations. (c) Theoretical and experimental STM images of the AgI surface ($U_s = -500$ mV). The ($\sqrt{79} \times \sqrt{79}$)R17.0° unit cell is indicated.

When optimizing the coordinates for the models with the buffer iodine layer, we found significant changes in the atomic structure—the flipping of one of the bilayers and the formation of a “sandwich”-like structure. This structure is based on two paired silver atomic planes to which one iodine plane adjoins on each side [Figs. 10(a) and 10(b)].

Figure 10(c) presents a theoretical STM image of the AgI surface obtained from DFT data in comparison with experimental one. One can see a good correspondence between the images. The remarkable feature of the structure is a low corrugation in STM images equaled to 0.2–0.3 Å directly measured experimentally and reproduced theoretically. This fact is in line with model drawings in Figs. 10(a) and 10(b) in which one can see that, in contrast to hexagonal phases, the atomic layers in a sandwich phase and a buffer layer are rather flat. The large z -distance between the sandwich structure and iodine buffer layer (≈ 4 Å) indicates weak van der Waals bonding. In other words, the sandwich phase is floating over the buffer layer.

It should be noted that the silver-terminated trial models of the AgI film have been also tested. They differ from the above-discussed models by the inverted sequence of Ag and I atomic layers. In all these cases, the structure also comes to the sandwich structure during the optimization of coordinates.

IV. DISCUSSION

A. Domain walls

In this work, we found that for the I/Ag(111) system, the transition from the commensurate $(\sqrt{3} \times \sqrt{3})R30^\circ$ phase to the incommensurate one begins due to uniaxial compression of the iodine lattice along the direction of the substrate atomic rows.

According to DFT data, iodine atoms in the $(\sqrt{3} \times \sqrt{3})R30^\circ$ phase occupy equivalent fcc positions. When compression starts, the atoms begin to move along atomic rows of the substrate. As a result, some part of atoms appear to be in bridge or hcp positions. At this stage, iodine atoms avoid to occupy on-top positions, as the least energetically favorable. As our experiments show, the compression is not uniform, as evidenced by the appearance of striped domain walls.

The formation of domain walls is a well-known mechanism of phase transition from a commensurate to an incommensurate phase, predicted theoretically,^{41,42} and studied in detail by diffraction methods for systems of noble gases physisorbed on the surface of metals or graphite.^{42–46} The possibility of the appearance of domain walls was first pointed out by Frenkel and Kontorova⁴⁷ using a simple one-dimensional model as an example. Domain walls are formed by atoms in which positions are not energetically favorable, but due to the fact that they separate domains in which the original commensurate structure is preserved, one can speak of a minimum energy for the system as a whole.

The formation of striped domain walls is a typical compression mechanism for halogen monolayers on the (111) surfaces of fcc metals. In particular, they were observed in the number of systems Cl/Cu(111),⁴⁸ I/Cu(111),⁴⁹ Cl/Ag(111),⁵⁰ I/Ni(111),⁵¹ and I/Au(111).⁵² Apparently, domain walls are also present for other systems [Br/Cu(111),⁵³ Cl/Ni(111)⁵⁴] in which typical LEED

patterns are observed, demonstrating triangles of six spots around the $\sqrt{3}$ -positions.

However, the situation with the formation of domain walls in the I/Ag(111) system needs to be explained in more detail. Indeed, sometimes it is difficult to distinguish a domain-wall system from the uniformly compressed one. They exhibit similar diffraction patterns and the periods of the superstructure. Although the nonuniformity of the structure follows from STM data, we agree that room temperature STM measurements that we present in Fig. 4 do not provide unambiguous proof of the domain-walls in the system, since the width of domain walls is close to the width of commensurate domains. Moreover, at finite temperature, the profile of domain walls becomes smoother than at 0 K, and the scanning at 300 K can cause additional fluctuations of the system due to atoms mobility or influence of the STM tip. Nevertheless, we insist to speculate about domain-walls in the system basing on the results of DFT calculations presented in Figs. 4(b) and 4(c). In the starting configuration, the iodine atoms were distributed uniformly within $(25 \times \sqrt{3}-R30^\circ)$ unit cell; however, the layer splits into $(\sqrt{3} \times \sqrt{3})R30^\circ$ domains and domain-walls after coordinates optimization. It is also noteworthy that the direct experimental proof of the domain-wall model was obtained for a number of halogen/Me(111) systems in which large domains of $(\sqrt{3} \times \sqrt{3})R30^\circ$ phase were found to be separated by domain-walls (not ordered yet) [I/Ni(111),⁵¹ Cl/Ag(111)⁵⁰]. It is likely that future low temperature STM measurements performed for the I/Ag(111) system can detect single domain walls at the coverage slightly exceeding 0.33 ML.

B. Hexagonal phases and rotational epitaxy

One of the interesting properties of the I/Ag(111) system is the presence of a first-order phase transition, during which the uniaxially compressed structure changes to a rotated hexagonal one. Similar phenomenon (called rotational epitaxy) was observed for both physisorbed^{11,13} and chemisorbed systems.⁵⁵

STM studies of the Xe/Pt(111) system showed that the rotated layer looks like a moiré pattern.^{56,57} The rotation of the adsorbate lattice can be represented as the rotation of hexagonal domain walls. This effect was theoretically predicted, in principle, by Villain⁵⁸ back in the 1980s. Tilted domain walls were experimentally obtained by Grimm *et al.*,⁵⁹ where the authors showed that the rotation of the xenon lattice on the graphite surface at 4 K is explained by the rotation of hexagonal domain walls separating domains with a commensurate structure.

Since the 1970s, a fairly large number of models have been proposed to explain rotational epitaxy. The most famous model was proposed by Novaco and McTague⁶⁰ and considers an incommensurate lattice. In the Doering model,⁶¹ it was shown that the stabilization of the angles of rotations occurs due to the formation of high-order commensurate structures with large periods. It was found in Shiba's work⁶² that during the transition from a commensurate to an incommensurate phase, a system of linear domain walls is first formed, which, starting from a certain critical value of the coating (the degree of compression of the monolayer), passes into a hexagonal incommensurate phase and a hexagonal incommensurate rotated phase. Different models predict qualitatively different dependencies of the turn angles on the degree of coverage. Basically, these theories describe the behavior of systems of physisorbed noble

gases for which the substrate potential is considered to be small, and the interaction potential between adsorbed atoms is considered to be well known. For systems such as alkali metals on metals⁶¹ and halogens on metals,⁵² where the interaction potential between the adsorbate and the substrate is sufficiently strong, the theoretical understanding of the mechanism of the rotational phase transitions was absent until recently.

It is noteworthy that all considered above models and approaches assume adsorption on the rigid substrate. In contrast, according to our STM and DFT data, a large violation of the substrate structure (11 layers in deep) takes place in the case of the I/Ag(111) system resulting in the noticeable corrugation of the surface (>1 Å). This result is a quite unexpected and, likely, is related with a new mechanism of the stress relief and needs to be investigated in detail in future works.

C. AgI structure

According to the result obtained in current and previous¹⁵ works, the interaction of molecular iodine with silver surfaces gives rise to the formation of the specific 2D sandwich-like AgI phase separated from the substrate by a buffer iodine layer.

Recently, exactly the same “sandwich”-structure was called the double-layer honeycomb structure.¹⁶ In particular, using DFT calculations, it was found that in the ultrathin limit (from one to several bilayers), the most stable form of semiconductors I–VII, II–VI, and III–V does not correspond to a truncated bulk structure but represents a “sandwich.”¹⁶ The DLHC-structure is not only kinetically stable, but for several bilayers, it is more energetically favorable than the structure obtained by simple truncation of the bulk phase. The stability of the DLHC-structure is due to the closure of dangling bonds in two paired layers in the middle of the structure. As a result, individual DLHC “sandwiches” can interact only through van der Waals forces, forming van der Waals crystals. Copper and silver halides (CuCl, CuBr, CuI, AgI), being I–VII semiconductors, form DLHC-type structures in the two-dimensional limit.^{16,63} Moreover, according to DFT calculations, for AgI and CuI, such a “sandwich” structure remains stable at a film thickness of up to ten layers.

To date, there are several detailed structural studies of thin halide films on metal surfaces performed for the systems exhibiting layer-by-layer (2D) growth at room temperature in ultra-high vacuum and in the electrochemical cell: CuBr/Cu(100),⁶⁴ CuI/Cu(111),^{36,65} CuI/Cu(100),^{36,66,67} CuI/Cu(110),³⁷ and AgI/Ag(100).¹⁵ In this view, the use of 2D metal halide films is quite promising for the creation of the van der Waals heterostructures on different substrates.

V. CONCLUSIONS

In summary, the interaction of molecular iodine with Ag(111) at 300 K has been studied with STM, LEED, AES, and DFT techniques. At the first stage of adsorption, iodine forms a simple monolayer with a $(\sqrt{3} \times \sqrt{3})R30^\circ$ structure. The DFT calculations indicated that iodine preferably occupies the fcc hollow adsorption sites. Further iodine dosing gives rise to compression of the iodine lattice and subsequent formation of silver iodide. The uniaxial compression of the chemisorbed iodine layer was found at $0.33 < \theta < 0.38$ ML. The structure of the compressed phase is explained in

terms of the striped super heavy domain-wall formation. The maximum compressed uniaxial phase is described by the $(13 \times \sqrt{3})R30^\circ$ unit cell. At $\theta > 0.38$ ML, the compressed rotated hexagonal phases characterized by a strong corrugation are formed. The nature of corrugation was found in the strong violation of the substrate lattice including up to ten atomic layers.

After saturation of the chemisorbed layer at $\theta = 0.43$ ML, iodide islands start growing near the step edges and defects. According to the DFT calculations, silver iodide forms the sandwich-like double-layer honeycomb¹⁶ structure, containing two coupled silver planes in the middle and iodine planes on each side. The “sandwich” as a whole is situated on top of the hexagonal buffer layer in which the density of iodine atoms is equal to their density in the sandwich.

SUPPLEMENTARY MATERIAL

See the [supplementary material](#) (video) for the AgI island growth on Ag(111) during iodine adsorption.

ACKNOWLEDGMENTS

We are grateful to the Joint Supercomputer Center of Russian Academy of Sciences for the use of using their computational resources for our calculations.

AUTHOR DECLARATIONS

Conflict of Interest

The authors have no conflicts to disclose.

DATA AVAILABILITY

The data that support the findings of this study are available from the corresponding author upon reasonable request.

APPENDIX: COMMENT ON A RECENT STM STUDY

After submission of the present paper, we found recently published paper by Dreyer *et al.*⁶⁸ in which iodine phases on Ag(111) were studied by low-temperature STM. The authors reported the observation of $(\sqrt{3} \times \sqrt{3})R30^\circ$, “triangular” and “hexagonal” phases. We believe that the “triangular” phase corresponds to our hex.-20 structure and “hexagonal” phase – to the AgI phase. The uniaxially compressed phases and the evolution of the period of the moire-like hexagonal phases, which take place in the narrow coverage range (0.33–0.43 ML), were not reported.

REFERENCES

- 1 R. G. Jones, *Prog. Surf. Sci.* **27**, 25 (1988).
- 2 E. I. Altman, in *Adsorbed Layers on Surfaces. Part 1: Adsorption on Surfaces and Surface Diffusion of Adsorbates*, edited by H. P. Bonzel (Springer, Berlin, 2001), Vol. 42A1, pp. 420–442.
- 3 B. V. Andryushechkin, T. V. Pavlova, and K. N. Eltsov, *Surf. Sci. Rep.* **73**, 83 (2018).
- 4 P. H. Citrin, P. Eisenberger, and R. C. Hewitt, *Phys. Rev. Lett.* **41**, 309 (1978).
- 5 P. H. Citrin, P. Eisenberger, and R. C. Hewitt, *J. Vac. Sci. Technol.* **15**, 449 (1978).
- 6 P. H. Citrin, P. Eisenberger, R. C. Hewitt, and H. H. Farrell, *J. Vac. Sci. Technol.* **16**, 537 (1979).

- ⁷U. Bardi and G. Rovida, *Surf. Sci.* **128**, 145 (1983).
- ⁸H. H. Farrell, M. M. Traum, N. V. Smith, W. A. Royer, D. P. Woodruff, and P. D. Johnson, *Surf. Sci.* **102**, 527 (1981).
- ⁹B. M. Ocko, O. M. Magnussen, J. X. Wang, R. R. Adžić, and T. Wandlowski, *Physica B* **221**, 238 (1996).
- ¹⁰T. Yamada, K. Ogaki, S. Okubo, and K. Itaya, *Surf. Sci.* **369**, 321 (1996).
- ¹¹E. D. Specht, A. Mak, C. Peters, M. Sutton, R. J. Birgeneau, K. L. D'Amico, D. E. Moncton, S. E. Nagler, and P. M. Horn, *Z. Phys. B: Condens. Matter* **69**, 347 (1987).
- ¹²M. D. Chinn and S. C. Fain, *Phys. Rev. Lett.* **39**, 146 (1977).
- ¹³K. Kern, R. David, P. Zeppenfeld, R. Palmer, and G. Comsa, *Solid State Commun.* **62**, 391 (1987).
- ¹⁴C. M. Lieber and X. L. Wu, *Acc. Chem. Res.* **24**, 170 (1991).
- ¹⁵B. V. Andryushechkin, G. M. Zhidomirov, K. N. Eltsov, Y. V. Hladchanka, and A. A. Korlyukov, *Phys. Rev. B* **80**, 125409 (2009).
- ¹⁶M. C. Lucking, W. Xie, D.-H. Choe, D. West, T.-M. Lu, and S. B. Zhang, *Phys. Rev. Lett.* **120**, 086101 (2018).
- ¹⁷E. R. Malinowski and D. G. Howery, *Factor Analysis in Chemistry* (Wiley, New York, 1980), p. 432.
- ¹⁸S. W. Gaarenstroom, *J. Vac. Sci. Technol.* **20**, 458 (1982).
- ¹⁹I. Horcas, R. Fernández, J. M. Gómez-Rodríguez, J. Colchero, J. Gómez-Herrero, and A. M. Baro, *Rev. Sci. Instrum.* **78**, 013705 (2007).
- ²⁰G. Kresse and J. Hafner, *Phys. Rev. B* **47**, 558 (1993).
- ²¹G. Kresse and J. Hafner, *Phys. Rev. B* **49**, 14251 (1994).
- ²²G. Kresse and J. Furthmüller, *Comput. Mater. Sci.* **6**, 15 (1996).
- ²³G. Kresse and J. Furthmüller, *Phys. Rev. B* **54**, 11169 (1996).
- ²⁴G. Kresse and D. Joubert, *Phys. Rev. B* **59**, 1758 (1999).
- ²⁵J. P. Perdew, K. Burke, and M. Ernzerhof, *Phys. Rev. Lett.* **77**, 3865 (1996).
- ²⁶H. J. Monkhorst and J. D. Pack, *Phys. Rev. B* **13**, 5188 (1976).
- ²⁷J. Tersoff and D. R. Hamann, *Phys. Rev. B* **31**, 805 (1985).
- ²⁸D. E. P. Vanpoucke and G. Brocks, *Phys. Rev. B* **77**, 241308 (2008).
- ²⁹A. Bondi, *J. Phys. Chem.* **68**, 441 (1964).
- ³⁰A. Gavezzotti, *J. Am. Chem. Soc.* **105**, 5220 (1983).
- ³¹R. Chauvin, *J. Phys. Chem.* **96**, 9194 (1992).
- ³²P. Zeppenfeld, K. Kern, R. David, and G. Comsa, *Phys. Rev. B* **38**, 3918 (1988).
- ³³T. Müller, D. Heuer, H. Pfnür, and U. Köhler, *Surf. Sci.* **347**, 80 (1996).
- ³⁴R. Dennert, M. Sokolowski, and H. Pfnür, *Surf. Sci.* **271**, 1 (1992).
- ³⁵Y. Wang, W. Wang, K. Fan, and J. Deng, *Surf. Sci.* **487**, 77 (2001).
- ³⁶B. V. Andryushechkin, K. N. Eltsov, and V. M. Shevlyuga, *Surf. Sci.* **566–568**, 203 (2004).
- ³⁷B. V. Andryushechkin, K. N. Eltsov, and V. V. Cherkov, *JETP Lett.* **83**, 162 (2006).
- ³⁸N. S. Komarov, T. V. Pavlova, and B. V. Andryushechkin, *Phys. Chem. Chem. Phys.* **23**, 1896 (2021).
- ³⁹N. S. Komarov, T. V. Pavlova, and B. V. Andryushechkin, *J. Phys. Chem. C* **123**, 27659 (2019).
- ⁴⁰R. W. G. Wyckoff, *Crystal Structures* (Wiley, 1963).
- ⁴¹I. F. Lyuksyutov, A. G. Naumovets, and V. L. Pokrovsky, *Two-Dimensional Crystals* (Academic Press, Boston, 1992).
- ⁴²P. Bak, *Rep. Prog. Phys.* **45**, 587 (1982).
- ⁴³K. Kern and G. Comsa, *Modulated Structures of Adsorbed Rare Gas Monolayers* (Plenum Press, New York, 1991), pp. 41–65.
- ⁴⁴M. den Nijs, in *Phase Transitions and Critical Phenomena*, edited by C. Domb and J. Lebowitz (Academic Press, 1988), Vol. 12, pp. 219–333.
- ⁴⁵H. Freimuth, H. Wiechert, H. P. Schildberg, and H. J. Lauter, *Phys. Rev. B* **42**, 587 (1990).
- ⁴⁶J. Cui and S. C. Fain, *Phys. Rev. B* **39**, 8628 (1989).
- ⁴⁷O. M. Braun and Y. Kivshar, *The Frenkel-Kontorova Model: Concepts, Methods, and Applications* (Springer-Verlag, Berlin, 2004), p. 472.
- ⁴⁸B. V. Andryushechkin, K. N. Eltsov, and V. M. Shevlyuga, *Surf. Sci.* **470**, L63 (2000).
- ⁴⁹B. V. Andryushechkin, K. N. Eltsov, and V. M. Shevlyuga, *Surf. Sci.* **472**, 80 (2001).
- ⁵⁰B. V. Andryushechkin, V. V. Cherkov, B. Kierren, Y. Fagot-Revurat, D. Malterre, and K. N. Eltsov, *Phys. Rev. B* **84**, 205422 (2011).
- ⁵¹N. S. Komarov, T. V. Pavlova, and B. V. Andryushechkin, *Surf. Sci.* **651**, 112 (2016).
- ⁵²L. Huang, P. Zeppenfeld, S. Horch, and G. Comsa, *J. Chem. Phys.* **107**, 585 (1997).
- ⁵³R. G. Jones and M. Kadodwala, *Surf. Sci.* **370**, L219 (1997).
- ⁵⁴W. Erley and H. Wagner, *Surf. Sci.* **66**, 371 (1977).
- ⁵⁵D. L. Doering and S. Semancik, *Surf. Sci. Lett.* **175**, L730 (1986).
- ⁵⁶S. Horch, P. Zeppenfeld, and G. Comsa, *Appl. Phys. A* **60**, 147 (1995).
- ⁵⁷F. Brunet, R. Schaub, S. Fédrigo, R. Monot, J. Buttet, and W. Harbich, *Surf. Sci.* **512**, 201 (2002).
- ⁵⁸J. Villain, *Surf. Sci.* **97**, 219 (1980).
- ⁵⁹B. Grimm, H. Hövel, M. Pollmann, and B. Reihl, *Phys. Rev. Lett.* **83**, 991 (1999).
- ⁶⁰A. D. Novaco and J. P. McTague, *Phys. Rev. Lett.* **38**, 1286 (1977).
- ⁶¹D. L. Doering, *J. Vac. Sci. Technol. A* **3**, 809 (1985).
- ⁶²H. Shiba, *J. Phys. Soc. Jpn.* **46**, 1852 (1979).
- ⁶³X. Huang, L. Yan, Y. Zhou, Y. Wang, H.-Z. Song, and L. Zhou, *J. Phys. Chem. Lett.* **12**, 525 (2021).
- ⁶⁴C. Y. Nakamura and E. I. Altman, *Surf. Sci.* **424**, 244 (1999).
- ⁶⁵N. T. M. Hai, S. Huemann, R. Hunger, W. Jaegermann, K. Wandelt, and P. Broekmann, *J. Phys. Chem. C* **111**, 14768 (2007).
- ⁶⁶P. Broekmann, N. T. M. Hai, and K. Wandelt, *J. Appl. Electrochem.* **36**, 1241 (2006).
- ⁶⁷P. Broekmann, N. T. M. Hai, and K. Wandelt, *Surf. Sci.* **600**, 3971 (2006).
- ⁶⁸M. Dreyer, J. Murray, E. Frederick, and R. E. Butera, *Surf. Sci.* **721**, 122081 (2022).